

Article

# Circular Polarization near the Tight Focus of Linearly Polarized Light

Sergey S. Stafeev<sup>1,2,\*</sup> , Anton G. Nalimov<sup>1,2</sup> , Alexey A. Kovalev<sup>1,2</sup> , Vladislav D. Zaitsev<sup>1,2</sup>  
and Victor V. Kotlyar<sup>1,2</sup> 

<sup>1</sup> Laser Measurements Laboratory, IPSI RAS—Branch of the FSRC “Crystallography and Photonics” RAS, Molodogvardeyskaya 151, 443001 Samara, Russia; antonsmr@mail.ru (A.G.N.); alanko.ipsi@mail.ru (A.A.K.); zaicev-vlad@yandex.ru (V.D.Z.); kotlyar@ipsiras.ru (V.V.K.)

<sup>2</sup> Technical Cybernetics Department, Samara National Research University, Moskovskoye Shosse 34, 443086 Samara, Russia

\* Correspondence: sergey.stafeev@gmail.com

**Abstract:** We have considered the tight focusing of light with linear polarization. Using the Richards–Wolf formalism, it is shown that before and after the focal plane, there are regions in which the polarization is circular (elliptical). When passing through the focal plane, the direction of rotation of the polarization vector is reversed. If before the focus in a certain area there was a left circular polarization, then directly in the focus in this area there will be a linear polarization, and after the focus in a similar area there will be a right circular polarization. This effect allows linearly polarized light to be used to rotate dielectric microparticles with little absorption around their center of mass.

**Keywords:** polarization conversion; tight focusing; Richards–Wolf formula; Stokes vector; spin angular momentum



**Citation:** Stafeev, S.S.; Nalimov, A.G.; Kovalev, A.A.; Zaitsev, V.D.; Kotlyar, V.V. Circular Polarization near the Tight Focus of Linearly Polarized Light. *Photonics* **2022**, *9*, 196. <https://doi.org/10.3390/photonics9030196>

Received: 14 February 2022

Accepted: 16 March 2022

Published: 17 March 2022

**Publisher’s Note:** MDPI stays neutral with regard to jurisdictional claims in published maps and institutional affiliations.



**Copyright:** © 2022 by the authors. Licensee MDPI, Basel, Switzerland. This article is an open access article distributed under the terms and conditions of the Creative Commons Attribution (CC BY) license (<https://creativecommons.org/licenses/by/4.0/>).

## 1. Introduction

Sharp focusing of laser radiation is understood as the focusing of light by lenses with a high numerical aperture, and it is no longer possible to neglect the vector nature of the light wave. In this case, to calculate the light field at the focus, it is necessary to take into account all the components of the strength of the electric (or magnetic) field of the light wave. The classical formulas for calculating the light field in a sharp focus were obtained by Richards and Wolf in [1].

At present, a large number of works have been devoted to the sharp focusing of light. However, most of the works have been devoted to studying the behavior of the intensity at the focus, for example, obtaining focal spots of various shapes [2–7]. Much less work has been presented on the study of other characteristics of the light field, such as the energy flux (Poynting vector) [8–10], spin or orbital angular momentum [11–14]. We also note that the main attention of researchers has focused on the study of the behavior of light directly in focus; less attention has been paid to the behavior of light at some distance from the plane of sharp focus.

In this paper, the sharp focusing of linearly polarized light is considered. It is shown that, at a distance from the focal plane, regions arise in which the polarization ceases to be linear. In this case, when passing through the plane of focus, the direction of polarization in these regions changes to the opposite—in regions with right circular polarization, the direction changes to left circular and vice versa.

## 2. Theoretical background

In [1], expressions were obtained for the projections of the electric field strength vector at the focus of the aplanatic system. The Jones vector for an initial field with linear polarization directed along the  $y$ -axis has the form:

$$\mathbf{E}_{lin} = A(\theta) \begin{pmatrix} 0 \\ 1 \end{pmatrix} \tag{1}$$

and the projections of the vector of the electric field strength and magnetic field strength near the focus for the initial field (1) have the form:

$$\begin{aligned} E_x &= -iI_{2,2} \sin 2\varphi, \\ E_y &= -i(I_{0,0} - I_{2,2} \cos 2\varphi), \\ E_z &= -2I_{1,1} \sin \varphi, \\ H_x &= i(I_{0,0} + I_{2,2} \cos 2\varphi), \\ H_y &= iI_{2,2} \sin 2\varphi, \\ H_z &= 2I_{1,1} \cos \varphi, \end{aligned} \tag{2}$$

where

$$I_{\nu,\mu} = \left(\frac{\pi f}{\lambda}\right) \int_0^{\theta_0} \sin^{\nu+1}\left(\frac{\theta}{2}\right) \cos^{3-\nu}\left(\frac{\theta}{2}\right) \cos^{1/2}(\theta) A(\theta) e^{ikz \cos \theta} J_{\mu}(x) d\theta, \tag{3}$$

where  $\lambda$  is the wavelength of light,  $f$  is the focal length of the aplanatic system,  $x = kr \sin \theta$ ,  $J_{\mu}(x)$  is the Bessel function of the first kind, and  $NA = \sin \theta_0$  is the numerical aperture. The angle  $\varphi$  in Equation (2) is the conventional polar (or azimuthal) angle in the transverse planes, including the focal plane. A positive angle value increases counterclockwise from the horizontal  $x$ -axis. In the initial plane, the light field has only linear polarization directed along the vertical  $y$ -axis, and the Jones vector (1) does not depend on the polar angle  $\varphi$ . In Equations (2) and (3), angle  $\theta$  is the tilt angle of the rays to the optical axis,  $\theta_0$  is the maximal tilt angle, determining the numerical aperture NA,  $z$  is the direction of the optical axis,  $z = 0$  is the focal plane,  $k$  is the wavenumber of light,  $(x, y)$  are the Cartesian coordinates in the cross-sections of the light beam converging into the focus ( $x$  is the horizontal axis,  $y$  is the vertical axis). The initial amplitude function  $A(\theta)$  (suppose it is a real function) can be constant (plane wave) or in the form of a Gaussian beam. From (2), one can obtain the intensity distributions of each component of the electric vector.

$$\begin{aligned} I_x &= I_{2,2}^2 \sin^2(2\varphi), \\ I_y &= I_{0,0}^2 + I_{2,2}^2 \cos^2(2\varphi) - 2I_{0,0}I_{2,2} \cos(2\varphi), \\ I_z &= 4I_{1,1}^2 \sin^2(\varphi). \end{aligned} \tag{4}$$

We note that Equations (1)–(4) differ from the equations obtained in [1], since the initial field (1) is polarized along the  $y$ -axis, whereas in [1] the initial field was polarized along the  $x$ -axis. Although the initial light field (1) has only one component  $E_y$ , Maxwell’s equations indicate that, upon light propagation, all three components of the E-field appear. If the light field propagates at a small angle to the optical axis, then the other two field components ( $E_x$  and  $E_z$ ) are small and can be neglected. At tight focusing, the light propagates at large angles to the optical axis, so that all three components of the E-field (2) have a comparable value [15,16]. It can be seen from (4) that the intensity distribution  $I_x$  of the horizontal projection of the electric vector in the plane of focus has the form of four local maxima (light spots), the centers of which are located on a circle centered on the optical axis and lying on the rays emanating from the center at angles  $\varphi = \pi/4, 3\pi/4, 5\pi/4$  and  $7\pi/4$ .

The intensity distribution  $I_y$  has the form of an almost circular spot with a maximum on the optical axis  $I_y = I_{0,0}^2$ . The difference from the round shape of the spot arises from the fact that the distribution of intensity  $I_y$  along the vertical axis ( $\varphi = \pi/2$ ) is greater

$(I_y = (I_{0,0} + I_{2,2})^2)$  than along the horizontal axis ( $\varphi = 0, I_y = (I_{0,0} - I_{2,2})^2$ ). The intensity distribution (4) at the focus of the longitudinal component of the electric vector  $I_z$  has the form of two light spots, the centers of which lie on the vertical axis. This type of intensity distribution of electric vector individual components leads to the fact that the distribution of the total intensity at the focus has the form of an ellipse elongated along the vertical axis:

$$I = I_x + I_y + I_z = I_{0,0}^2 + I_{2,2}^2 + 2I_{1,1}^2 - 2(I_{1,1}^2 + I_{0,0}I_{2,2}) \cos(2\varphi). \tag{5}$$

Let us find the longitudinal component of the spin angular momentum (SAM) vector near the field focus (1) using the formula [17]:

$$\mathbf{S} = \left( \frac{c^2 \epsilon_0}{2\omega} \right) \text{Im}(\mathbf{E}^* \times \mathbf{E}) \tag{6}$$

where  $c$  is the speed of light in vacuum,  $\omega$  is the angular frequency of the monochromatic light,  $\epsilon_0$  is the vacuum permittivity,  $\text{Im}$  is the imaginary part of the number,  $\times$  is the sign of vector multiplication,  $*$  is the sign of complex conjugation. Below, we omit the constant  $[(c^2 \epsilon_0) / (2\omega)]$  for brevity. We note that sometimes, due to the electric–magnetic democracy, Equation (6) is written with two terms rather than one:  $[c^2 / (2\omega)] \text{Im}[\epsilon_0(\mathbf{E}^* \times \mathbf{E}) + \mu_0(\mathbf{H}^* \times \mathbf{H})]$ , with  $\mu_0$  being the vacuum permeability ( $c^2 \epsilon_0 = \mu_0^{-1}$ ). However, immediately from the expression for the Poynting vector, only one term is obtained either for the E-vector or for the H-vector [17]. In addition, due to their different constants, both terms will give different contribution to the components of the SAM vector. Thus, Expression (6) is correct. Substituting from (2) into (6), we will assume that integrals (3) are complex, since  $z$  is different from zero. We get:

$$S_z = 2\text{Im}(E_x^* E_y) = 2 \sin(2\varphi) \text{Im}(I_{2,2}^*(I_{0,0} - \cos(2\varphi) I_{2,2})) \tag{7}$$

Certainly, near the tight focus, all 6 components of the E- and H-vectors (2) are significant, and none of these components can be neglected. Therefore, similarly to Equation (7), we can write expressions for the components  $S_x$  and  $S_y$ :

$$\begin{aligned} S_x &= 2\text{Im}(E_y^* E_z) = 4 \sin(\varphi) \text{Re}\left(I_{1,1} \left( \cos(2\varphi) I_{2,2}^* - I_{0,0}^* \right)\right), \\ S_y &= 2\text{Im}(E_z^* E_x) = 4 \sin(\varphi) \sin(2\varphi) \text{Re}\left(I_{1,1}^* I_{2,2}\right). \end{aligned} \tag{8}$$

Let us single out the real and imaginary parts of the integrals included in (7)  $I_{0,0} = R_0 + iI_0, I_{2,2} = R_2 + iI_2$ . Then, instead of (7), we write:

$$S_z = 2 \sin(2\varphi) (I_0 R_2 - I_2 R_0) \tag{9}$$

The integrals  $R_0, R_2$  in (9) include the comultiplier  $\cos(kz \cos \theta) \approx 1$  at  $kz \ll 1$ , and the integrals  $I_0, I_2$  include the comultiplier  $\sin(kz \cos \theta) \approx kz \sin \theta$  at  $kz \ll 1$ . With this in mind, instead of (9), we write:

$$S_z \approx 2kz \sin(2\varphi) (\bar{I}_0 \bar{R}_2 - \bar{I}_2 \bar{R}_0) \tag{10}$$

In (10), the following notations are used:

$$\begin{aligned} \bar{R}_0 &= I_{0,0}(z=0), \bar{R}_2 = I_{2,2}(z=0), \\ \bar{I}_0 &= I_{0,0}(z=0), \bar{I}_2 = I_{2,2}(z=0), \\ \bar{I}_{\nu,\mu} &= \left( \frac{\pi f}{\lambda} \right) \int_0^{\theta_0} \sin^{\nu+1} \left( \frac{\theta}{2} \right) \cos^{3-\nu} \left( \frac{\theta}{2} \right) \cos^{3/2}(\theta) A(\theta) e^{ikz \cos \theta} J_\mu(x) d\theta. \end{aligned} \tag{11}$$

Let, on a circle of some radius, the expression in parentheses in (10) be greater than zero  $\bar{I}_0 \bar{R}_2 - \bar{I}_2 \bar{R}_0 > 0$ , and since  $\sin(2\varphi)$  in (10) is positive in quadrants 1 and 3, and negative in 2 and 4, then before the focus ( $z < 0$ ) the longitudinal component SAM  $S_z$  in

(10) will be positive in quadrants 2 and 4, and negative in 1 and 3. Moreover, since the sign of the entire expression after the focus ( $z > 0$ ) changes to the opposite, the longitudinal component of SAM  $S_z$  in (9) is positive in quadrants 1 and 3, and negative in 2 and 4. This means that before the focus in the quadrants 2 and 4, the polarization vector rotates counterclockwise (right circular or elliptical polarization), and after the focus in these quadrants, the polarization vector rotates clockwise (left circular or elliptical polarization). Recall that in the plane of focus, the light at each point only has linear polarization, since at  $z = 0$  the longitudinal component of the SAM  $S_z$  in (10) is equal to zero. The defocusing magnitude  $z$  in Equation (10) affects the size of the areas in the transverse plane, where polarization is not linear. At a distance  $z$  nearly equal to  $\lambda$ , the size of the circular polarization area is maximal (for  $NA = 0.95$  it is approximately  $\lambda/2$ ). As  $z$  tends to zero (i.e., in the focus), the size of the area with circular polarization decreases to zero.

Note also that the longitudinal component of the SAM is exactly equal to the third component of the Stokes vector:

$$S_z = 2\text{Im}(E_x^* E_y) = s_3, \tag{12}$$

which shows the presence of circular and elliptical polarization in the light field. In the next section, the presented theoretical predictions will be confirmed by simulation.

We note that the change in the rotation direction of the polarization vector to the opposite beyond the focal plane, as follows from Equation (10), can be explained by the angular momentum (AM) conservation law. Since polarization in the initial plane and in the focal plane is locally linear,  $S_z = 0$ . Therefore, if there are areas with left-handed circular polarization before the focus, then beyond the focus, circular polarization in these areas should become right-handed. However, the presence of such areas near the focus does not follow from the AM conservation.

### 3. Simulation by Richards–Wolf Formula

In this work, using the Richards–Wolf formulas, the focusing of a linearly polarized plane wave (wavelength 633 nm) was simulated by choosing a lens with  $NA = 0.95$ . The field near the tight focus was calculated using the integrals [1]:

$$\begin{aligned} \mathbf{U}(\rho, \psi, z) = & -\frac{if}{\lambda} \int_0^{\theta_0} \int_0^{2\pi} B(\theta, \varphi) T(\theta) \mathbf{P}(\theta, \varphi) \times \\ & \times \exp\{ik[\rho \sin \theta \cos(\varphi - \psi) + z \cos \theta]\} \sin \theta \, d\theta \, d\varphi, \end{aligned} \tag{13}$$

where  $\mathbf{U}(\rho, \psi, z)$  is the strength of the electric or magnetic field,  $B(\theta, \varphi)$  is the electric or magnetic field at the input of the wide-aperture system in coordinates of the exit pupil ( $\theta$  is the polar angle,  $\varphi$  is the azimuthal angle),  $T(\theta)$  is the lens apodization function,  $f$  is the focal length,  $k = 2\pi/\lambda$  is the wavenumber,  $\lambda$  is the wavelength (in the simulation it was considered equal to 633 nm) and  $\alpha_{\max}$  is the maximum polar angle determined by the numerical aperture of the lens ( $NA = \sin \theta_0$ );  $\mathbf{P}(\theta, \varphi)$  is the polarization vector, for the strength of the electric and magnetic fields has the form:

$$\mathbf{P}(\theta, \varphi) = \begin{bmatrix} 1 + \cos^2 \varphi (\cos \theta - 1) \\ \sin \varphi \cos \varphi (\cos \theta - 1) \\ -\sin \theta \cos \varphi \end{bmatrix} a(\theta, \varphi) + \begin{bmatrix} \sin \varphi \cos \varphi (\cos \theta - 1) \\ 1 + \sin^2 \varphi (\cos \theta - 1) \\ -\sin \theta \sin \varphi \end{bmatrix} b(\theta, \varphi), \tag{14}$$

where  $a(\theta, \varphi)$  and  $b(\theta, \varphi)$  are functions describing the polarization state of the  $x$ - and  $y$ -components intensities of the focused beam. In contrast to Equations (2) and (3), we gave Equations (13) and (14) in a general form to show that further modeling is carried out by the general Equations (13) and (14) and that the simulation results confirm the theoretical conclusions, following from Equations (11) and (12). After calculating the components of

the electric field, the behavior of the components of the Stokes vector near the sharp focus were determined. The Stokes vector components were calculated using the formulas:

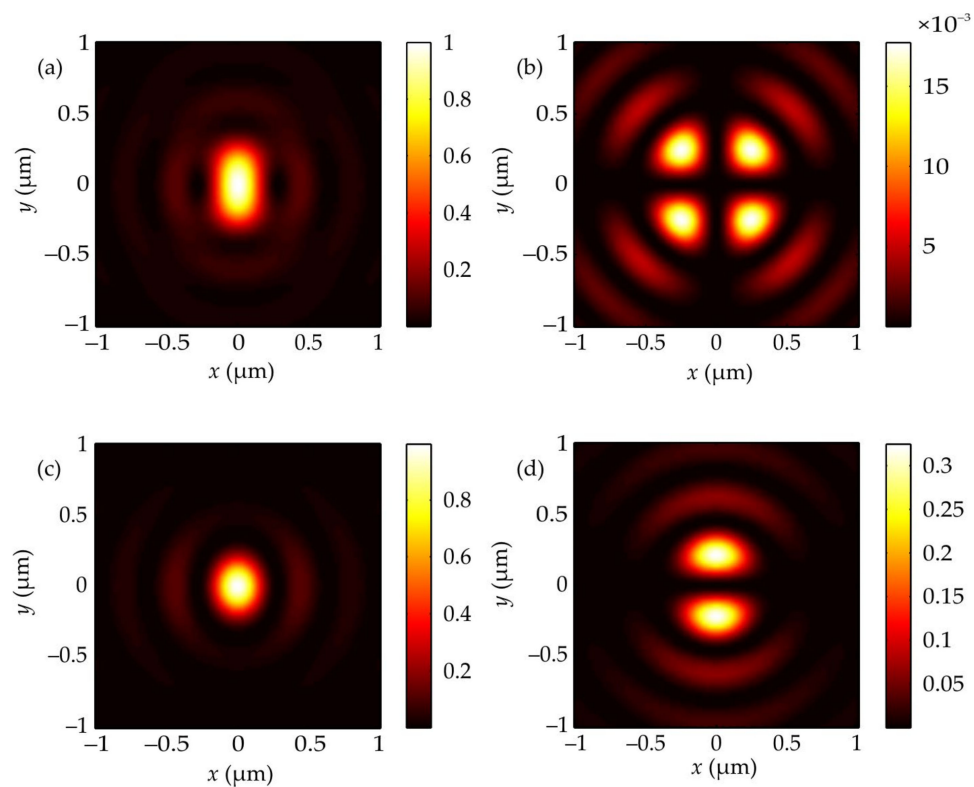
$$\begin{aligned}
 s_0 &= E_x E_x^* + E_y E_y^*, \\
 s_1 &= E_x E_x^* - E_y E_y^*, \\
 s_2 &= 2\text{Re}(E_x^* E_y), \\
 s_3 &= 2\text{Im}(E_x^* E_y).
 \end{aligned}
 \tag{15}$$

Similarly to Equations (7)–(9), the substitution of Equation (2) into Equation (15) allows us to obtain explicit expressions for the Stokes components  $s_1$  and  $s_2$  near the focus. For instance, a simpler expression is derived for  $s_2$  at  $kz \ll 1$ :

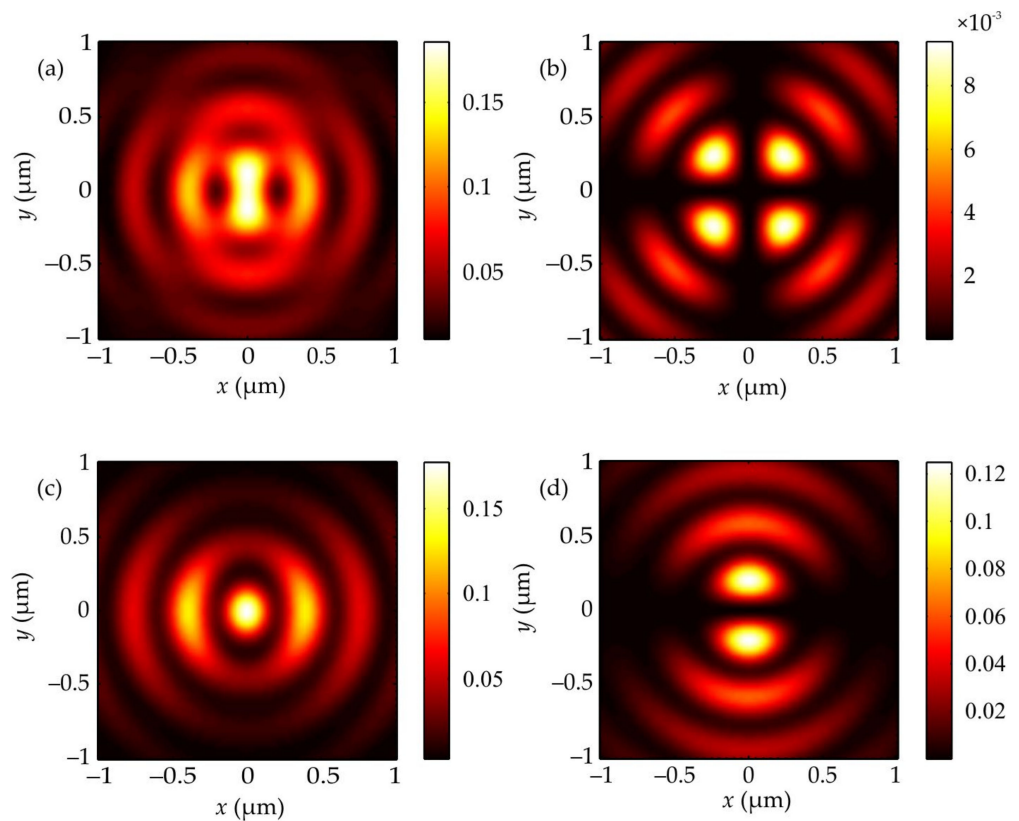
$$s_2 \approx 2 \sin(2\varphi) \bar{R}_2 (\bar{R}_0 - \bar{R}_2 \cos(2\varphi))
 \tag{16}$$

At small  $kz \ll 1$ , the second Stokes component (16) does not depend on  $z$  and therefore does not change sign when passing through the focus ( $z = 0$ ). Below, this is confirmed by simulation. Similarly, the first Stokes component  $s_1$  in Equation (15), expressed via the components of the E-vector (2), is also independent of  $z$  near the focus.

To estimate the relative contribution of individual polarization components, it is convenient to use the Stokes vector components normalized to the transverse intensity:  $(S_1, S_2, S_3) = (s_1/s_0, s_2/s_0, s_3/s_0)$ . It is known that when focusing light of linear polarization at the focus, all three components of the electric field strength are observed [18]. Figure 1 illustrates the distribution of the total intensity and its individual components in the focus of an aplanatic lens with  $\text{NA} = 0.95$ , when focusing a plane wave with a wavelength of 633 nm and polarization along the  $y$ -axis. To estimate the effect of defocusing, Figure 2 shows the same distributions of the total intensity and of the individual intensity components as in Figure 1, but at a distance  $\lambda$  from the focal plane. The intensity distributions have the same shape at the same distance before and after the focus.



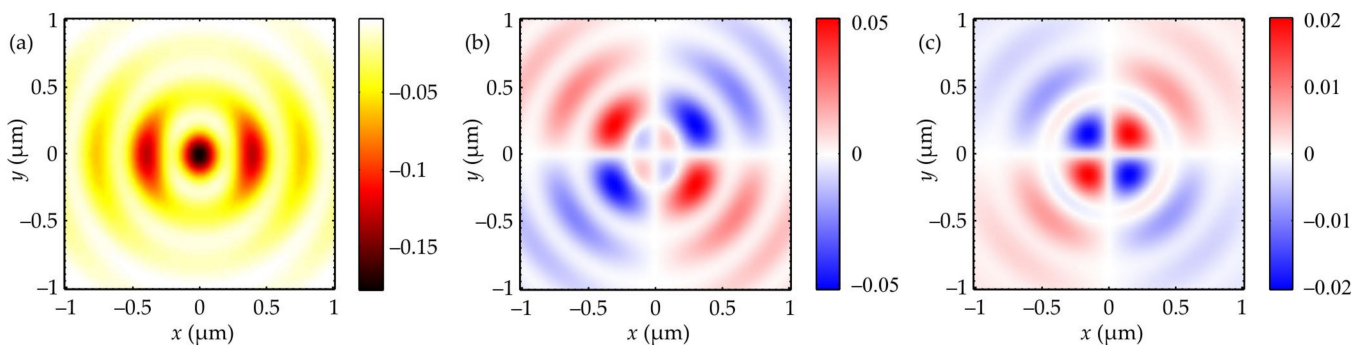
**Figure 1.** Distribution of the total intensity  $I_x + I_y + I_z$  (a) and individual components of the intensity  $I_x$  (b),  $I_y$  (c),  $I_z$  (d) in the plane of focus.



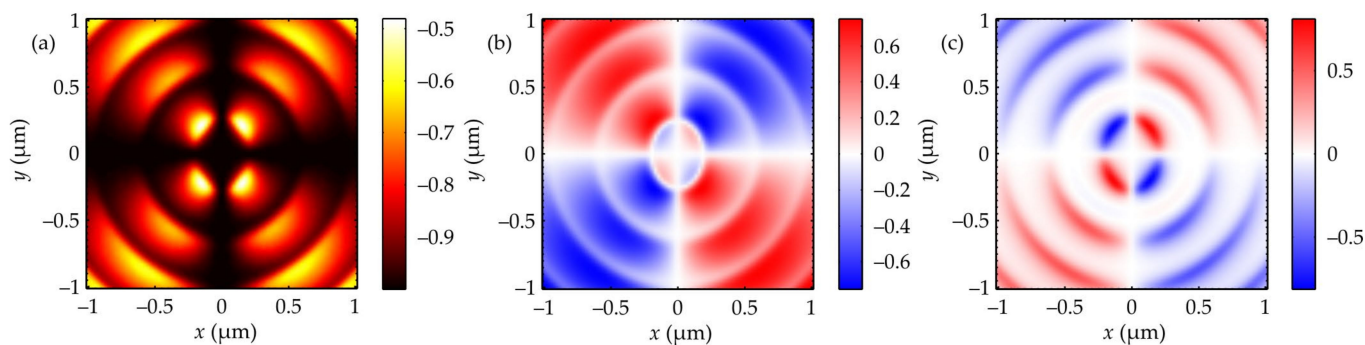
**Figure 2.** Distribution of the total intensity  $I_x + I_y + I_z$  (a) and individual components of the intensity  $I_x$  (b),  $I_y$  (c),  $I_z$  (d) at a distance  $\lambda$  after the focus.

Figure 1 shows that the initial component makes the main contribution to the focal spot formation, but the longitudinal component of the intensity also begins to make a significant contribution. The component perpendicular to the input polarization is rather small but present, while the light at the focus is still linearly polarized. Note that the distributions of the total intensity at the focus and the intensity of individual components in Figure 1 confirm the theoretical predictions that follow from Equations (4) and (5). Figure 2 indicates that a small shift from the focal plane (by a distance  $\lambda$ ) leads to a decrease of the maximum intensity five times.

The distribution of the components of the Stokes vector ( $s_1, s_2, s_3$ ) and the normalized components of the Stokes vector ( $S_1, S_2, S_3$ ) at the distance  $z = \lambda$  after the focus is shown in Figures 3 and 4, respectively.



**Figure 3.** Distribution of the Stokes vector components  $s_1$  (a),  $s_2$  (b) and  $s_3$  (c) at a distance  $\lambda$  after the focus.



**Figure 4.** Distribution of the components of the normalized Stokes vector  $S_1$  (a),  $S_2$  (b) and  $S_3$  (c) at a distance  $\lambda$  after the focus.

From Figures 3 and 4, it can be seen that the polarization after focus is predominantly linear. In the center of the focal spot in Figure 3a, a minimum is observed, which indicates that the polarization at the focus is directed along the  $y$  axis. This is also confirmed by Figure 4a: for a wave fully polarized along the  $y$ -axis  $S_1 = -1$ . From Figure 4a, it can be seen that the polarization does not change its direction at the focus and along the  $x$  and  $y$  axes, but along the straight lines located at an angle of  $\pm 45^\circ$  to the axes, the deviation from the initial polarization turns out to be maximum. From Figures 3 and 4, it is also seen that the diverging beam contains regions with circular polarization. Recall that there are no such regions at the focus itself—the light is linearly polarized. From Figure 4c it is seen that the contribution of the circular polarization in such regions is quite noticeable—for  $S_3 = \pm 1$ , the polarization is completely circular, but there, in some regions,  $S_3$  reaches values of  $\pm 0.8$ .

Figures 5 and 6 similarly show the distribution of the Stokes vector and normalized Stokes vector at a distance of one wavelength in front of the focus.

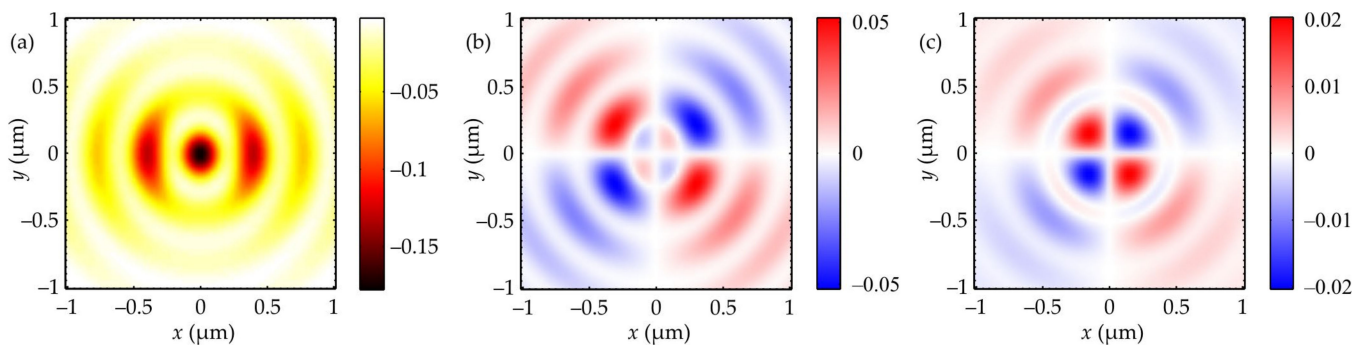


**Figure 5.** Stokes vector components  $s_1$  (a),  $s_2$  (b), and  $s_3$  (c) at a distance  $\lambda$  before the focal plane.

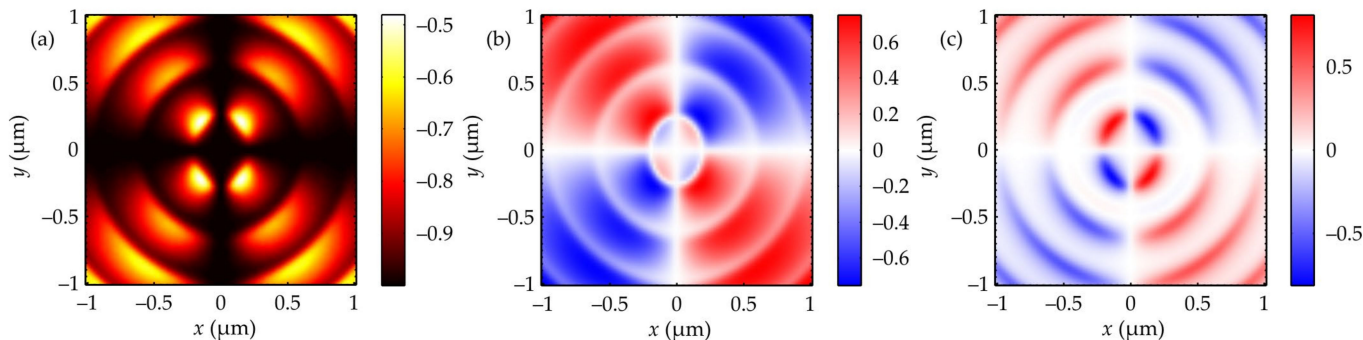


**Figure 6.** Distribution of the components of the normalized Stokes vector  $S_1$  (a),  $S_2$  (b) and  $S_3$  (c) at a distance  $\lambda$  before the focal plane.

A comparison of Figures 4–6 shows that the first two components of the Stokes vector describing the linear polarization have not changed, and the third has changed its sign to the opposite. After passing the plane of the focus, the direction of the circular (elliptical) polarization is reversed—for example, in the first quadrant, the light in front of the focus plane had a left circular polarization, and after focus, a right polarization. Before the focus, the right circular (elliptical) polarization appears in the second and fourth quadrants and the left circular polarization appears in the first and third quadrants (Figure 6c). It agrees with the theoretical prediction based on Expression (10), and the change in the direction of rotation of the polarization vector in these quadrants after passing through the focus also follows from (10).

Below, we show how the distribution of  $S_3$  changes with the distance from the focal plane. Figure 7 shows the intensity distribution (Figure 7a) and the longitudinal Stokes component  $S_3$  (Figure 7b) in the longitudinal plane  $yz$  along the  $z$ -axis, rotated by an angle  $\phi = 45^\circ$  (i.e., passing through the  $S_3$  maximum in Figure 6).

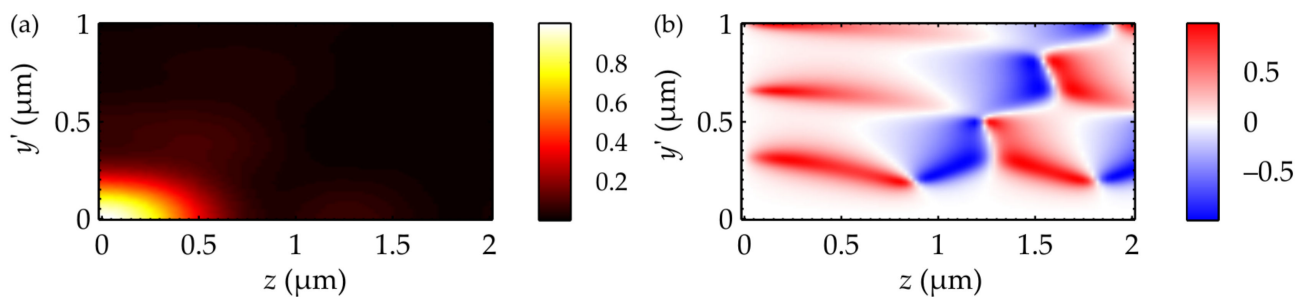


**Figure 7.** Distributions of the intensity (a) and of the third Stokes component (b) in the longitudinal plane  $yz$  along the  $z$ -axis (by an angle  $45^\circ$  degrees).

Figure 7 demonstrates that in the focal plane, the light field is linearly polarized. However, directly beyond the focal plane, areas with an elliptical polarization are generated (red areas in Figure 7). It is also interesting that as we move away from the focus, the direction of rotation of the polarization vectors changes to the opposite (blue areas in Figure 7). Figure 7b also shows how the size of the area with elliptical polarization changes with the distance  $z$ .

#### 4. Modeling the Formation of Circular Polarization Using the FDTD Method

To check the correctness of the calculations by the Richards–Wolf formulas, an additional simulation was performed using the FDTD method. The focusing of a linearly polarized plane wave ( $\lambda = 633 \text{ nm}$ ) by a Fresnel zone plate with a focal length of  $f = 500 \text{ nm}$  and a diameter of  $7.9 \mu\text{m}$  was considered. The numerical aperture of such a lens is  $\text{NA} = 0.99$ . The focusing was simulated using the FDTD method implemented in FullWave software. Note that the FDTD method implemented in FullWave makes it possible to calculate the values of the electromagnetic field components at individual moments of time. To calculate the complex amplitude on the basis of individual instantaneous values of the field amplitudes, the method proposed in [19] was used. Figure 8 shows the distribution of the components of the normalized Stokes vector at a distance of one wavelength after the focus.

From Figure 8, it can be seen that simulating using the FDTD method confirms the results obtained using the Richards–Wolf formulas. In particular, Figure 8a shows that light is predominantly linearly polarized along the  $y$ -axis, and Figure 8c shows that quadrants 1 and 3 contain a right-handed circular polarization, and quadrants 2 and 4 a left-handed circular polarization.

Comparison of Figures 4 and 8 indicates that although the structures of both patterns are similar, there are also significant differences. This is because the simulations by the Richards–Wolf method [1] and by the FDTD method [19] were carried out under different conditions. In the latter case, the tight focusing of light was simulated by passing the



light field through a real Fresnel zone plate with a focal length equal to the wavelength ( $f = \lambda$ ) and with a numerical aperture  $NA = 0.99$ . At the same time, the Richards–Wolf formalism adequately describes the light field at the focus of an ideal spherical lens if  $f \gg \lambda$ . Thus, the Richards–Wolf formalism approximately describes the behavior of light near the focus, whereas the FDTD method, based on a rigorous solution of the Maxwell equations, adequately describes the behavior of light at the focus near the surface of the focusing zone plate. Therefore, modeling by the FDTD method expands the boundaries of the discovered optical phenomenon: a generation of local areas with circular (elliptical) polarization near the tight focus of light with initially linear polarization.

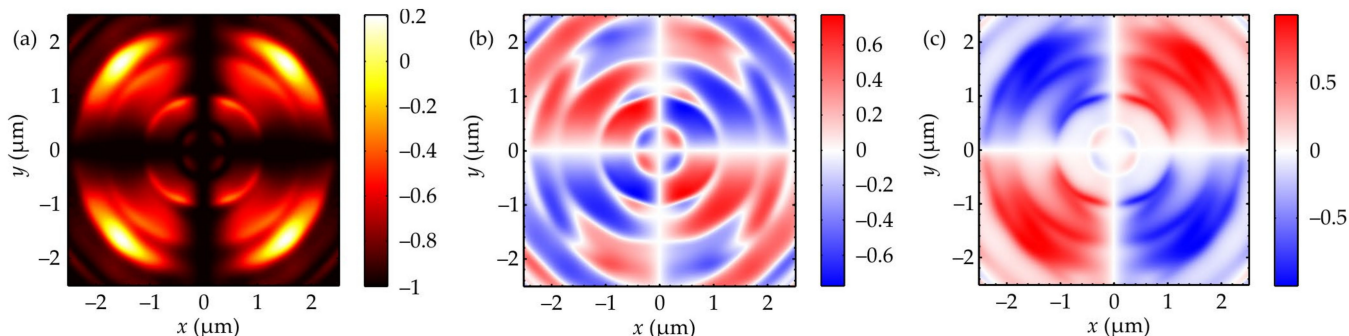


**Figure 8.** Components of the Stokes vector  $S_1$  (a),  $S_2$  (b) and  $S_3$  (c) when calculating using FullWAVE software at a distance of  $0.65 \mu\text{m}$  after the actual focus.

### 5. Reducing the Contribution of Circular Polarization with Decreasing Numerical Aperture of the Lens

Let us now consider the contribution of reducing the numerical aperture of the lens to  $NA = 0.6$  (corresponding to a standard  $40\times$  aplanatic lens). The result is shown in Figure 9. Figure 9 shows that the maximum  $S_3$  has decreased by two times. Moreover, from Figure 9a, it can be seen that the relative contribution of the linear polarization (along the y axis) increased significantly: the maximum in Figure 4 was equal to  $-0.5$ , and in Figure 9a to  $-0.92$ . Recall that for  $S_1 = \pm 1$ , the polarization is completely linear.

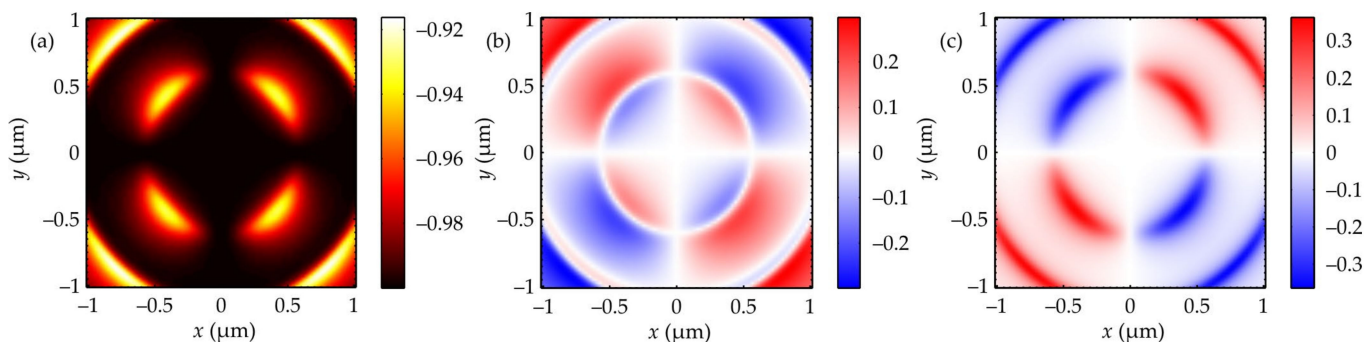


**Figure 9.** Distribution of the components of the normalized Stokes vector  $S_1$  (a),  $S_2$  (b) and  $S_3$  (c) for a lens with a numerical aperture  $NA = 0.6$ .

### 6. Calculation of the Moment of Forces Acting on a Dielectric Microparticle near the Focus

Let us calculate a force and a torque, acting onto a microbead from the light field. The force  $\mathbf{F}$  and the torque  $\mathbf{M}$  relative to an arbitrary point  $A$ , are equal to [20,21].

$$\mathbf{F} = - \oint_S (\boldsymbol{\sigma} \cdot \mathbf{n}) dS \tag{17}$$

$$\mathbf{M} = \oint_S [\mathbf{r} \times (\boldsymbol{\sigma} \cdot \mathbf{n})] dS \tag{18}$$

where  $\mathbf{r}$  is the radius-vector from the point A ( $x,y,z$ ) to the point of integration on the surface  $S$ ,  $\mathbf{n}$  is an external normal vector to the surface  $S$ , A is the point relative to which the torque  $\mathbf{M}$  is calculated and  $\boldsymbol{\sigma}$  is the Maxwell stress tensor, the components of which in the CGS system can be written as [22]

$$\sigma_{ik} = \frac{1}{4\pi} \left( \frac{|\mathbf{E}|^2 + |\mathbf{H}|^2}{2} \delta_{ik} - E_i E_k - H_i H_k \right) \tag{19}$$

where  $E_i, H_i$  are the electric and magnetic field components and  $\delta_{ik}$  is the Kronecker symbol ( $\delta_{i=k} = 1, \delta_{i \neq k} = 0$ ).

Shown in Figure 10 is a simulation result of the torque and force calculation acting on the spherical microbead.

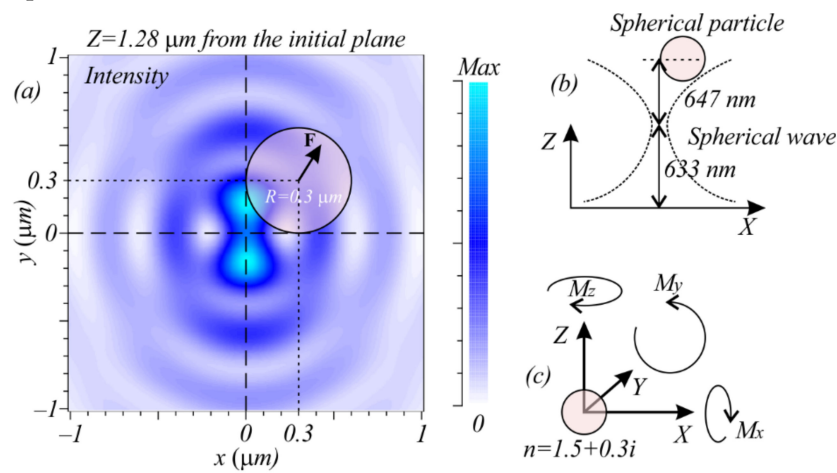


**Figure 10.** Intensity pattern (a) and a spherical bead with radius  $R = 0.3 \mu\text{m}$ . The position of the bead is  $X_p = 0.3 \mu\text{m}, Y_p = 0.3 \mu\text{m}$ . Shown at the right are a schematic position of the bead (b) and directions of the positive torque values along the  $x, y$  and  $z$  axis (c).

Calculations show, that for the position of the particle  $X_p = 0.3 \mu\text{m}, Y_p = 0.3 \mu\text{m}$  the force projections are  $F_x = 2.79 \text{ pN}, F_y = 3.7 \text{ pN}$  and  $F_z = 8.78 \text{ pN}$ . The torque projections are  $M_x = 2.81 \cdot 10^{-19} \text{ Nm}, M_y = -5.55 \cdot 10^{-19} \text{ Nm}$  and  $M_z = 1.73 \cdot 10^{-19} \text{ Nm}$ . If we shift the bead at the position  $X_p = 0.3 \mu\text{m}, Y_p = -0.3 \mu\text{m}$ , then the result force projections become  $F_x = 2.66 \text{ pN}, F_y = -3.58 \text{ pN}$  and  $F_z = 8.9 \text{ pN}$ , and the torque projections become  $M_x = -3.0 \cdot 10^{-19} \text{ Nm}, M_y = -5.9 \cdot 10^{-19} \text{ Nm}$  and  $M_z = -1.5 \cdot 10^{-19} \text{ Nm}$ . Figure 10 shows that in the first quadrant, the axial torque is positive ( $M_z = 1.73 \cdot 10^{-19} \text{ Nm}$ ), and in the fourth quadrant the torque is negative ( $M_z = -1.5 \cdot 10^{-19} \text{ Nm}$ ). This proves that the longitudinal projection of the CAM is positive in the first quadrant and negative in the fourth (Figures 8 and 9).

### 7. Conclusions

In this work, theoretically, using the Richards–Wolf formalism and using two different modeling methods, it was shown that with the sharp focusing of light with a linear polarization in the planes before and after the focus, there were regions that arose in pairs in even and odd quadrants, and in these regions, light was circularly or elliptically polarized (for example, even to the right and odd to the left). Moreover, after passing through the focus in these areas, the direction of rotation of the polarization vector changes to the opposite (in even quadrants, it becomes left-handed, and in odd quadrants, it becomes right-handed circular or elliptical polarization). This result allows the use of linearly polarized light to

rotate microparticles (the size of the circularly polarized region is about  $0.3\ \mu\text{m}$  by  $0.3\ \mu\text{m}$ ) around its center of mass.

We note that a similar result has been obtained in [23]. It has been shown that certain structures allow the generation before the focus and beyond the focus of two conjugate optical vortices with opposite-sign topological charges and with longitudinal axial polarization. In our work, we have not used any additional structures.

**Author Contributions:** Conceptualization, S.S.S. and V.V.K.; methodology, S.S.S. and V.V.K.; software, S.S.S. and V.D.Z.; validation, V.V.K.; formal analysis, S.S.S. and V.V.K.; investigation, S.S.S., V.D.Z., A.G.N., A.A.K. and V.V.K.; resources, S.S.S.; data curation, S.S.S.; writing—original draft preparation, S.S.S. and V.D.Z.; writing—review and editing, A.G.N., A.A.K. and V.V.K.; visualization, S.S.S. and A.G.N.; supervision, V.V.K.; project administration, V.V.K.; funding acquisition, S.S.S. All authors have read and agreed to the published version of the manuscript.

**Funding:** This work was supported by the Russian Science Foundation (Project No. 18-19-00595) in parts of “Theoretical background” and Ministry of Science and Higher Education within the State assignment FSRC “Crystallography and Photonics” RAS in part of “Numerical simulation”.

**Institutional Review Board Statement:** Not applicable.

**Informed Consent Statement:** Not applicable.

**Data Availability Statement:** Not applicable.

**Conflicts of Interest:** The authors declare no conflict of interest.

## References

1. Richards, B.; Wolf, E. Electromagnetic diffraction in optical systems, II. Structure of the image field in an aplanatic system. *Proc. R. Soc. Lond. Ser. A Math. Phys. Sci.* **1959**, *253*, 358–379. [[CrossRef](#)]
2. Yuan, G.H.; Wei, S.B.; Yuan, X.-C. Nondiffracting transversally polarized beam. *Opt. Lett.* **2011**, *36*, 3479–3481. [[CrossRef](#)] [[PubMed](#)]
3. Ping, C.; Liang, C.; Wang, F.; Cai, Y. Radially polarized multi-Gaussian Schell-model beam and its tight focusing properties. *Opt. Express* **2017**, *25*, 32475–32490. [[CrossRef](#)]
4. Grosjean, T.; Gauthier, I. Longitudinally polarized electric and magnetic optical nano-needles of ultra high lengths. *Opt. Commun.* **2013**, *294*, 333–337. [[CrossRef](#)]
5. Wang, H.; Shi, L.; Lukyanchuk, B.; Sheppard, C.; Chong, C.T. Creation of a needle of longitudinally polarized light in vacuum using binary optics. *Nat. Photon* **2008**, *2*, 501–505. [[CrossRef](#)]
6. Lin, J.; Chen, R.; Jin, P.; Cada, M.; Ma, Y. Generation of longitudinally polarized optical chain by  $4\pi$  focusing system. *Opt. Commun.* **2015**, *340*, 69–73. [[CrossRef](#)]
7. Zhuang, J.; Zhang, L.; Deng, D. Tight-focusing properties of linearly polarized circular Airy Gaussian vortex beam. *Opt. Lett.* **2020**, *45*, 296–299. [[CrossRef](#)]
8. Lyu, Y.; Man, Z.; Zhao, R.; Meng, P.; Zhang, W.; Ge, X.; Fu, S. Hybrid polarization induced transverse energy flow. *Opt. Commun.* **2020**, *485*, 126704. [[CrossRef](#)]
9. Li, H.; Wang, C.; Tang, M.; Li, X. Controlled negative energy flow in the focus of a radial polarized optical beam. *Opt. Express* **2020**, *28*, 18607. [[CrossRef](#)]
10. Kotlyar, V.V.; Stafeev, S.S.; Nalimov, A.G. Energy backflow in the focus of a light beam with phase or polarization singularity. *Phys. Rev. A* **2019**, *99*, 033840. [[CrossRef](#)]
11. Bomzon, Z.; Gu, M.; Shamir, J. Angular momentum and geometrical phases in tight-focused circularly polarized plane waves. *Appl. Phys. Lett.* **2006**, *89*, 241104. [[CrossRef](#)]
12. Aiello, A.; Banzer, P.; Neugebauer, M.; Leuchs, G. From transverse angular momentum to photonic wheels. *Nat. Photon.* **2015**, *9*, 789–795. [[CrossRef](#)]
13. Li, M.; Cai, Y.; Yan, S.; Liang, Y.; Zhang, P.; Yao, B. Orbit-induced localized spin angular momentum in strong focusing of optical vectorial vortex beams. *Phys. Rev. A* **2018**, *97*, 053842. [[CrossRef](#)]
14. Zhao, Y.; Edgar, J.S.; Jeffries, G.; McGloin, D.; Chiu, D.T. Spin-to-Orbital Angular Momentum Conversion in a Strongly Focused Optical Beam. *Phys. Rev. Lett.* **2007**, *99*, 073901. [[CrossRef](#)] [[PubMed](#)]
15. Monteiro, P.B.; Neto, P.A.M.; Nussenzveig, H.M. Angular momentum of focused beams: Beyond the paraxial approximation. *Phys. Rev. A* **2009**, *79*, 033830. [[CrossRef](#)]
16. Bekshaev, A. A simple analytical model of the angular momentum transformation in strongly focused light beams. *Open Phys.* **2010**, *8*, 947–960. [[CrossRef](#)]
17. Berry, M.V. Optical currents. *J. Opt. A Pure Appl. Opt.* **2009**, *11*, 094001. [[CrossRef](#)]

18. Gross, H.; Singer, W.; Totzeck, M. *Handbook of Optical Systems*; Gross, H., Singer, W., Totzeck, M., Eds.; Wiley: Hoboken, NJ, USA, 2005; Volume 2, ISBN 9783527403783.
19. Golovashkin, D.L.; Kazanskiy, N.L. Mesh domain decomposition in the finite-difference solution of Maxwell's equations. *Math. Model. Comput. Simul.* **2009**, *18*, 203–211. [[CrossRef](#)]
20. Rockstuhl, C.; Herzig, H.P. Calculation of the torque on dielectric elliptical cylinders. *J. Opt. Soc. Am. A* **2005**, *22*, 109–116. [[CrossRef](#)]
21. Nalimov, A.G.; Kotlyar, V.V. Calculation of the moment of the force acting by a cylindrical Gaussian beam on a cylindrical microparticle. *Comput. Opt.* **2007**, *31*, 16–20. [[CrossRef](#)]
22. Landau, L.D.; Lifshitz, E.M. *The Classical Theory of Fields*; Nauka: Moscow, Russia, 1973. (In Russian)
23. Man, Z.; Xi, Z.; Yuan, X.; Burge, R.E.; Urbach, H.P. Dual Coaxial Longitudinal Polarization Vortex Structures. *Phys. Rev. Lett.* **2020**, *124*, 103901. [[CrossRef](#)] [[PubMed](#)]